Bulletin of the Seismological Society of America, 91, 4, pp. 651–666, August 2001

A Theoretical Omega-Square Model Considering Spatial Variation in Slip and Rupture Velocity. Part 2: Case for a Two-Dimensional Source Model

by Yoshiaki Hisada

Abstract The theoretical basis of the ω-squared model and the characteristics of near-source broadband strong ground motions are investigated using a 2D source model with spatial variations in slip and rupture velocity. This is an extension of a study by Hisada (2000a), who used 1D source models for the same purpose. First, Hisada's slip-velocity function (2000a) is modified by superposing scalene triangles to construct Kostrov-type slip-velocity functions with arbitrary combinations for the source-controlled f_{max} and the slip duration. Then, it is confirmed that the Fourier amplitudes of these slip velocities fall off as the inverse of ω at frequencies lower than f_{max} (Hisada, 2000a). Next, the effects of 2D spatial distributions of slip and rupture time on the source spectra are investigated. In order to construct a realistic slip distribution, the hybrid slip model is proposed, which is the combination of the asperity model at lower wavenumbers and the *k*-squared model (Herrero and Bernard, 1994) at higher wavenumbers. The source spectra of the proposed 2D models, which have the *k*-squared distribution for slip and rupture time, fall off as the inverse of ω, when the slip is instantaneous. This result also agrees with Hisada (2000a). Therefore, the ω-inverse-squared model, which consists of the combination of the Kostrov-type slip velocity proposed here and the *k*-squared distributions for both slip and rupture time, is not only consistent with the empirical ω-squared model, but also provides the theoretical basis for constructing realistic 2D source models at broadband frequencies. In addition, it is confirmed that the proposed source model successfully simulates most of the well-known characteristics of the near-fault strong ground motions at broadband frequencies, that is, permanent offsets in displacements, long-period pulses in velocities, and complex randomness in accelerations. The near-source directivity effects are also confirmed; the fault-normal components are dominant over the fault-parallel components, especially at the forward rupture direction. However, the ratio between the fault-normal and fault-parallel components is roughly independent of frequency, which is contradictory to empirical models. This suggests that a 3D faulting model is necessary to represent more realistic near-source strong motions at broadband frequencies.

Introduction

Hisada (2000a) proposed the ω-inverse-squared model by modifying the *k*-squared model of Herrero and Bernard (1994) and Bernard *et al.* (1996) to construct ω-squared source models (Aki, 1967, 1972). The *k*-squared model is based on the three assumptions that (1) the spatial wavenumber spectrum of the slip distribution falls off as the inverse of the wavenumber squared (*k*-squared), (2) the Fourier amplitudes of the slip velocity are independent of ω at high frequencies, and (3) the rupture velocity is constant.

Hisada (2000a) modified the last two assumptions. First, as a more realistic slip velocity, a Kostrov-type slip velocity model (Kostrov, 1964; Nakamura and Miyatake, 2000), which has a sharp rise and a relatively smooth decay, was proposed by superposing isosceles triangles with different durations (I used the term *equilateral triangles* in Hisada (2000a) by mistake). After checking the Fourier amplitudes of various slip models, Hisada (2000a) found that (1) this model had two corner frequencies, the first (f_1) corresponding to the total slip duration (roughly the reciprocal of twice the total duration) and the second to the source-controlled f_{max} (roughly the reciprocal of the minimum duration among triangles), and (2) the Fourier amplitude of the slip velocity fell off as the inverse of ω between f_1 and f_{max}.

Second, in order to investigate the effects of variable

rupture velocity on source spectra, Hisada (2000a) introduced the incoherent rupture time (Δt_r), namely, the difference between the actual rupture time and the coherent rupture time. Using 1D unilateral source models, Hisada (2000a) found that (1) the *k*-squared distribution for Δt_r was the most plausible among *k*-inversed, *k*-squared, and *k*-cubed distributions, and (2) the source spectra fell off as the inverse of ω when combining those models with the instantaneous slip and the *k*-squared slip distribution.

Finally, Hisada (2000a) proposed the ω-inverse-squared model, which consists of the combination of the two ω-inverse models, the slip velocity proposed previously and the *k*-squared spatial distributions in slip and Δt_r, and confirmed that it was consistent with the empirical ω-squared model.

In this article, I improve my previous model (Hisada, 2000a) using 2D source models and more flexible slip-velocity functions. First, I briefly introduce the formulation of the source spectra using 2D fault models. Second, I generalize Hisada's slip-velocity model by superimposing scalene triangles, and I check its Fourier amplitude. I introduce empirical relations to find appropriate relations among the parameters for constructing the slip velocities. Third, I investigate the effects of the spatial variation of slip and rupture time on the source spectra using 2D source models. Fourth, I simulate broadband strong motions near a fault to check waveforms (accelerations, velocities, and displacements) and, especially, the directivity effects. The main effect of the rupture directivity is the increase of the long-period ground motion in the direction normal to the fault plane (e.g., Aki, 1968). However, empirical models show this effect disappears at intermediate to high frequencies (e.g., Somerville *et al.,* 1995). Thus, it is interesting to see whether the proposed source model explains this phenomenon or not. Finally, I discuss the validity and the merits and demerits of the ω-inverse-squared model.

Formulation of 2D Source Models and Source Spectra

The displacements (U_i) at an observation station (Y) from a source model can be written as follows using a 2D source model (e.g., Aki and Richards, 1980),

$$U_i(Y;\,\omega) = \int_0^W \int_0^L \{\mu D(\mathbf{e}_k\mathbf{n}_j + \mathbf{e}_j\mathbf{n}_k)U^*_{ik,j}\cdot\exp(i\omega\cdot t_r)\}dx_1dx_2, \quad (1)$$

where Y is an observation point, ω is the circular frequency, W and L are the width and length of the fault, respectively, μ is the rigidity ($= \sqrt{V_S/\rho}$), D is the slip distribution, $\mathbf{e}_k$ and $\mathbf{n}_j$ are the slip- and fault-normal vectors, respectively, $U^*_{ik,j}$ is the derivative of Green's function along the *j*th direction, and t_r is the rupture time (see Fig. 1). Following Hisada (2000a), the far-field displacements in a homogeneous full-space can be simplified as follows:

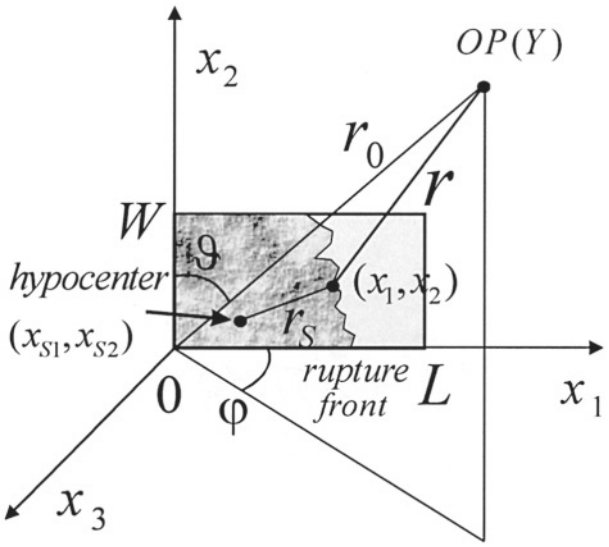

Figure 1. Geometry of a 2D source model and the coordination system, together with an observation point.

$$U_i(Y;\,\omega) = \frac{R_i}{4\pi\rho rc^3}M_0(\omega), \quad (2)$$

where the subscript *i* denotes the *i*th component in the spherical coordinate system, and R_i is the radiation pattern for the *i*th component. The variable c is the medium velocity (V_P for the radial and V_S for the transverse and vertical directions), ρ is the density, and r is the distance from the rupture front (x_1, x_2) to Y. M_0 in equation (2) is the source spectrum and is expressed as

$$M_0(\omega) = \mu \int_0^W \int_0^L D(x_1,\,x_2)F_V(x_1,\,x_2;\,\omega) \exp\{i\omega(t_c + t_r)\}dx_1dx_2, \quad (3)$$

where F_V is the Fourier transform of the slip-velocity function, whose integration corresponds to the unit dislocation, and t_c is the arrival time of the seismic waves from the rupture front to the observation point.

The arrival time and the rupture time are given as

$$t_c(x_1,\,x_2) = \frac{r}{c} \approx \frac{r_0 - x_1\sin\theta\cos\varphi - x_2\cdot\cos\theta}{c} \quad (x_1,\,x_2 \ll r_0), \quad (4)$$

and

$$t_r(x_1, x_2) = \frac{r_S}{\overline{V}r} + \Delta t_r(x_1, x_2), \tag{5}$$

$$\text{with} \quad r_S(x_1, x_2) = \sqrt{(x_1 - x_{S1})^2 + (x_2 - x_{S2})^2}, \tag{6}$$

where r_0 is the distance from the origin of the fault plane to Y, θ and φ are the location of Y in spherical coordinates, $\overline{V}_r$ is the constant rupture velocity, and x_{S1} and x_{S2} are the locations of the hypocenter (the starting point of the rupture). Following Hisada (2000a), I divide the rupture time t_r into the coherent rupture time ($r_s/\overline{V}_r$) and the incoherent rupture time (Δt_r). I introduce Δt_r to represent the fluctuations at rupture front due to the variable rupture velocity.

Substituting equations (4), (5), and (6) into equation (3), the following source spectrum is obtained:

$$M_0(\omega) = \mu \exp\left(i\omega \frac{r_0}{c}\right) \int_0^W \int_0^L D(x_1, x_2) F_V(x_1, x_2; \omega) \exp\left\{i\omega\left(\frac{r_S}{\overline{V}rC_d} + \Delta t_r\right)\right\} dx_1 dx_2, \tag{7}$$

where, C_d is the directivity coefficient of the 2D source model,

$$C_d = \frac{1}{1 - \dfrac{\overline{V}r}{c}\left(\dfrac{x_1}{r_S}\cos\theta + \dfrac{x_2}{r_S}\sin\theta\cos\varphi\right)}. \tag{8}$$

When $\theta = 90°$, equation (8) becomes the directivity coefficient of the 1D source model (Ben-Menahem, 1961).

As seen in (7), the source spectra are controlled by the spatial distributions of the static slip, the slip-velocity function, and the rupture time. In the following, I first check the Fourier amplitudes of the slip velocity function and then the effects of the spatial variations of the slip and the rupture time on the source spectra.

Fourier Amplitudes of Slip-Velocity Functions

Following Hisada (2000a), I express the slip-velocity function (F_v) as a function with a sharp rise and a relatively smooth decay, which can be obtained by superimposing triangles with different durations. The combination of triangles from short to long durations guarantees broadband frequency contents. While Hisada (2000a) used isosceles triangles as element triangles for the simplicity, I will generalize the formulation using scalene triangles to utilize arbitrary combinations of slip durations and f_{max}.

In the time domain, the slip-velocity function superposing scalene triangles can be written as follows (see Fig. 2):

$$F_V(x_1, x_2; t) = \frac{1}{A}\sum_{i=1}^{N_V} Ar^{j-1}\cdot \dot{f}_j(t) \quad \text{with } A = \sum_{j=1}^{N_V} Ar^{j-1}, \tag{9}$$

where N_V is the total number of triangles, and Ar is the ratio of the area of the $j + 1$th triangle with respect to the area of the jth triangle (i.e., $Ar = A_{j+1}/A_j$).

In equation (9), $\dot{f}_j$ is the scalene triangle of the jth element,

$$\dot{f}_j(t) = \begin{cases} A_{1j}\cdot t, & (0 \le t \le \tau_{1j}) \\ A_{2j}\cdot(\tau_j - t), & (\tau_{1j} \le t \le \tau_j), \\ 0, & (\tau_j \le t) \end{cases} \tag{10}$$

$$\text{with} \quad A_{1j} = V_j/\tau_{1j},\ A_{2j} = V_j/\tau_{2j} \text{ and } V_j = 2/\tau_j, \tag{11}$$

where A_{1j}, A_{2j}, and V_j are the absolute values of the maximum and minimum accelerations and maximum velocity of the jth triangle, respectively. The variables τ_{1j}, τ_{2j}, and τ_j are the first-half, the second-half, and the total durations of the jth triangle, respectively. They are defined as follows:

$$\tau_j = \tau_{min}\cdot Tr^{j-1},\ \tau_{1j} = \frac{\tau_i}{Tr}, \text{ and } \tau_{2j} = \tau_j - \tau_{1j},\ (j = 1, 2, 3, \ldots, N_V) \tag{12}$$

$$\text{with } \tau_{min} \equiv \tau_1 = \frac{1}{f_{max}}, \text{ and } \tau_{max} \equiv \tau_{N_V} = \frac{Tr^{N_V-1}}{f_{max}} \tag{13}$$

where Tr is the ratio of τ_{j+1} with respect to τ_j and is also the ratio of τ_j to τ_{1j} (i.e., $Tr = \tau_{j+1}/\tau_j = \tau_j/\tau_{1j}$; see Fig. 2). The reciprocal of the minimum duration (τ_1) corresponds to the source-controlled f_{max} (Hisada, 2000a), and τ_{max} is the total duration of the slip. For the case of the isosceles triangle, Tr is 2 (see equation 19 of Hisada [2000a]).

The slip displacement and acceleration are obtained by replacing $\dot{f}_j$ in equation (9) by

$$f_j(t) = \begin{cases} \dfrac{t^2}{\tau_j\tau_{1j}}, & (0 \le t \le \tau_{1j}) \\ \dfrac{\tau_{1j}\tau_{2j} + (t-\tau_{1j})(\tau_{2j}+\tau_j-t)}{\tau_j\tau_{2j}}, & (\tau_{1j} \le t \le \tau_j), \\ 1, & (\tau_j \le t) \end{cases} \tag{14}$$

for displacement, and

$$\ddot{f}_j(t) = \begin{cases} A_{1j}, & (0 \le t \le \tau_{1j}) \\ -A_{2j}, & (\tau_{1j} \le t \le \tau_j) \\ 0 & (\tau_j \le t) \end{cases} \tag{15}$$

for acceleration.

The Fourier transform of equation (9) can be obtained analytically:

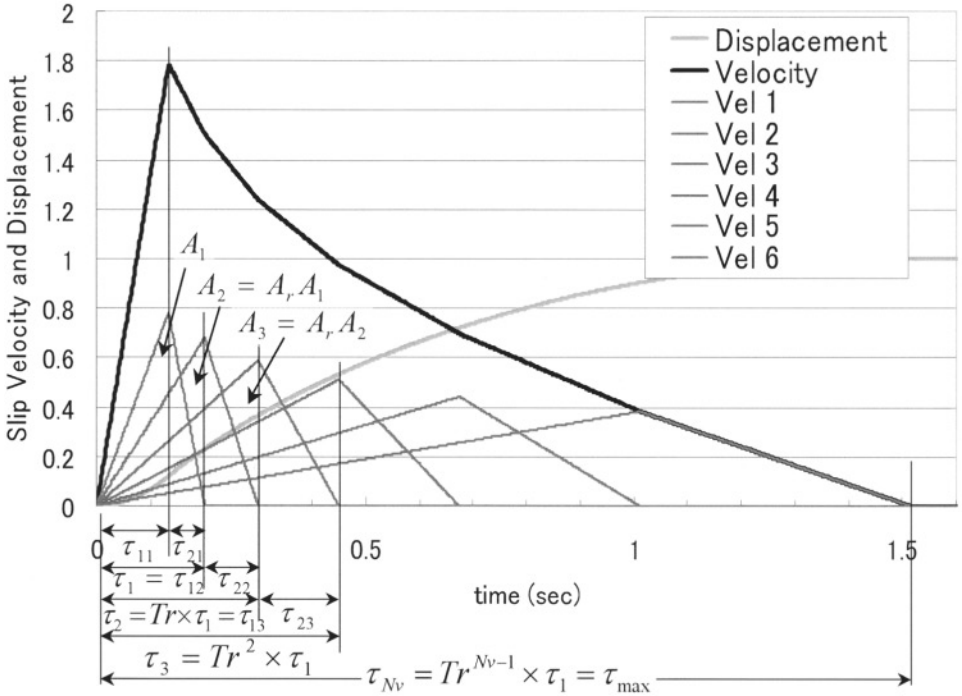

Figure 2. The slip-velocity function (black line) and the corresponding slip displacement (thick gray line). The velocity function consists of several isosceles triangles with various durations (six triangles in thin lines in this case).

$$F_{\mathrm{V}}(x_1, x_2; \omega) = \frac{1}{A} \sum_{j=1}^{N_{\mathrm{V}}} A r^{j-1} \cdot \dot{f}_j(\omega), \tag{16}$$

where

$$\dot{f}_j(\omega) = i \frac{\exp(i\chi_{1j})}{\chi_j} \left(\frac{\sin \chi_{1j}}{\chi_{1j}} - \frac{\sin \chi_{2j}}{\chi_{2j}} \exp(i\chi_j) \right), \tag{17}$$

$$\text{with} \quad \chi_j = \frac{\omega \cdot \tau_j}{2}, \ \chi_{1j} = \frac{\omega \cdot \tau_{1j}}{2}, \ \chi_{2j} = \frac{\omega \cdot \tau_{2j}}{2}, \tag{18}$$

and i is the imaginary number.

Although the parameters $f_{\max}$ ($=1/\tau_1$), Ar, Tr, and N_{V} in the slip-velocity function can be arbitrary, I roughly estimate their relations for a given magnitude by considering empirical relations and then check the Fourier amplitudes of the plausible slip velocities.

First, according to Sato (1979), who compiled the source parameters of Japanese earthquakes, the following empirical relations were obtained between magnitude, M, and fault length, L, and between M and average slip, $\bar{D}$:

$$\log_{10} L(\mathrm{km}) = 0.5M - 1.88, \tag{20}$$

$$\log_{10} \bar{D}(\mathrm{cm}) = 0.5M - 1.4 \ . \tag{21}$$

In addition, Geller (1976) obtained the following empirical relation between fault length and slip duration (rise time).

$$\tau_{\max}(\mathrm{sec}) = 0.0726L(\mathrm{km}) \tag{22}$$

On the other hand, Somerville *et al.* (1999) derived the similar relations using more recent source inversion results, as follows:

$$\bar{D}(\mathrm{cm}) = 1.56 \cdot 10^{-7} \cdot M_0^{1/3}, \tag{23}$$

$$\tau_{\max}(\mathrm{sec}) = 2.03 \cdot 10^{-9} \cdot M_0^{1/3} \tag{24}$$

where M_0 is the seismic moment. Therefore, when we combine the previous equations with a magnitude–seismic moment relation, such as that of Hanks and Kanamori (1979),

$$M = \frac{2}{3} \log_{10} M_0 - 10.7, \tag{25}$$

we obtain the other set of empirical relations among magnitude, the average slip, and the slip duration.

The left columns in Table 1 show relations for various M values vs. the corresponding combinations of $\tau_{\max}$ and $\bar{D}$ using equations (20)–(22) by Sato and Geller and equations (23)–(25) by Somerville *et al.* (1999). As for $f_{\max}$, I tested three cases: 10, 5, and 1 Hz. Although $\bar{D}$ values are comparable between the relations by Sato (1979) and Somerville *et al.* (1999), $\tau_{\max}$ values obtained by Geller (1976) are about two times larger than those obtained by Somerville *et al.* (1999). This is probably caused by the different datasets and frequency bands between the two relations; especially

Table 1
Maximum Slip Velocities and Accelerations Using Various Magnitudes (M), f_{max} Values, and Ar Values

f_{max} = 10 Hz and Tr = 1.77

	Sato *et al.*		Somerville *et al.*			Ar = 1.2		Ar = 1.4		Ar = 1.6		Ar = 1.77		Ar = 2	
M	τ (sec)	D(cm)	τ (sec)	D(cm)	Nv	V_{max}	A_{max}	V_{max}	A_{max}	V_{max}	A_{max}	V_{max}	A_{max}	V_{max}	A_{max}
4.0	0.1	4.0	0.05	3.5	1	**78**	**1416**	78	1416	78	1416	78	1416	78	1416
4.5	0.2	7.1	0.08	6.2	2	87	1580	83	1515	80	1460	78	1420	76	1373
5.0	0.3	13	0.14	11	3	106	1934	**96**	**1738**	88	1580	82	1469	75	1345
5.5	0.6	22	0.26	20	4	127	2301	105	1903	89	1603	79	1404	68	1197
6.0	1.0	40	0.45	35	5	168	3059	127	2297	99	1767	81	1443	67	1129
6.5	1.7	71	0.81	62	6	225	4090	153	2761	107	1919	82	1447	67	1029
7.0	3.1	126	1.4	110	7	308	5591	187	3369	118	2097	82	1451	66	929
7.5	5.4	224	2.6	196	8	429	7786	231	4161	129	2307	82	1457	66	836
8.0	9.6	398	4.5	349	9	604	10980	288	5179	443	2545	83	1463	66	749

f_{max} = 5 Hz and Tr = 1.74

	Sato *et al.*		Somerville *et al.*			Ar = 1.2		Ar = 1.4		Ar = 1.6		Ar = 1.74		Ar = 2	
M	τ (sec)	D(cm)	τ (sec)	D(cm)	Nv	V_{max}	A_{max}	V_{max}	A_{max}	V_{max}	A_{max}	V_{max}	A_{max}	V_{max}	A_{max}
4.5	0.2	7.1	0.08	6.2	1	71	618	71	618	71	618	71	618	71	618
5.0	0.3	13	0.14	11	2	82	718	79	689	76	665	75	650	72	626
5.5	0.6	22	0.26	20	3	94	817	85	736	77	671	73	632	66	573
6.0	1.1	40	0.45	35	4	**120**	**1047**	100	870	84	735	76	661	64	553
6.5	1.8	71	0.81	62	5	157	1362	118	1028	91	795	77	674	63	513
7.0	3.2	126	1.4	110	6	209	1822	**142**	**1237**	99	865	79	687	64	470
7.5	5.6	224	2.6	196	7	287	2496	174	1513	109	949	81	702	65	427
8.0	9.7	398	4.5	349	8	399	3475	215	1869	**120**	**1044**	82	717	66	386

f_{max} = 1 Hz and Tr = 1.76

	Sato *et al.*		Somerville *et al.*			Ar = 1.2		Ar = 1.4		Ar = 1.6		Ar = 1.76		Ar = 2	
M	τ (sec)	D(cm)	τ (sec)	D(cm)	Nv	V_{max}	A_{max}	V_{max}	A_{max}	V_{max}	A_{max}	V_{max}	A_{max}	V_{max}	A_{max}
6.0	1.0	40	0.45	35	1	80	−185	80	−185	80	−185	80	−185	80	−185
6.5	1.8	71	0.81	62	2	89	158	84	148	86	151	81	142	78	137
7.0	3.1	126	1.4	110	3	106	187	91	161	96	169	81	143	74	131
7.5	5.5	224	2.6	196	4	133	234	101	178	110	194	82	145	70	123
8.0	9.6	398	4.5	349	5	173	305	114	201	130	229	83	146	68	113

The average slip (D) and the slip duration (τ) are empirically derived by Sato (1979) and Geller (1976). As a reference, the more recent results by Somerville *et al.* (1999) are also shown. The lightly shaded areas indicate the maximum values within realistic ranges. In particular, the bold values in the heavily shaded areas indicate values used to calculate Fourier amplitudes of the slip accelerations, as shown in Figure 4.

Geller's relations were based on mainly longer-period seismograms from large-scale offshore earthquakes, whereas those of Somerville *et al.* (1999) were based on mainly shorter-period strong motions from small- to medium-scale inland earthquakes. As shown in Figures 2 and 3, the slip-velocity functions used in this study are broadband; the beginnings of the slips excite the high-frequency waves, and the subsequent slips are coda with decreasing amplitudes, which contribute only to low-frequency waves. Therefore, I use the relations by Sato (1979) and Geller (1976) as slip-velocity functions in this study. In this case, the values of Tr are similar from 1.74 to 1.77 among the three f_{max} values, as shown in Table 1.

The right columns of Table 1 show the maximum (or minimum) values of slip velocities and accelerations. As for Ar, several values between 1.2 and 2 are tested. The shaded areas in Table 1 indicate the maximum accelerations and velocities within realistic ranges, that is, about 50 to 200 (cm/sec) for peak velocities, and 500 to 2000 (gal) for peak accelerations. The values of 200 (cm/sec) and 2000 (gal) for peak velocities and accelerations, respectively, may seem too high for using the average slips. However, it should be noted that the durations for the peak values are extremely short, that is, instantaneous for the velocities and $\tau_{11}(\approx 0.5/f_{max})$ for the accelerations. In addition, they are raw values without material damping, scattering, and frequency-band limits.

Figure 3a and b shows the slip velocities and the Fourier amplitudes of the corresponding slip accelerations. Only results for f_{max} = 5 Hz are shown because the results for all the other cases are similar. The slip velocities are Kostrov-type functions (namely, a sharp rise and a smooth decay) for $Tr > Ar$, scalene triangles for $Tr = Ar\ (= 1.74)$, and smooth functions without sharp peaks for $Tr < Ar$. Accordingly, the Fourier amplitudes for the larger Ar show the smaller amplitudes at high frequencies. Similar to Hisada (2000a), the Fourier amplitudes have two corner frequencies; the first is nearly equal to the reciprocal of twice of the slip duration,

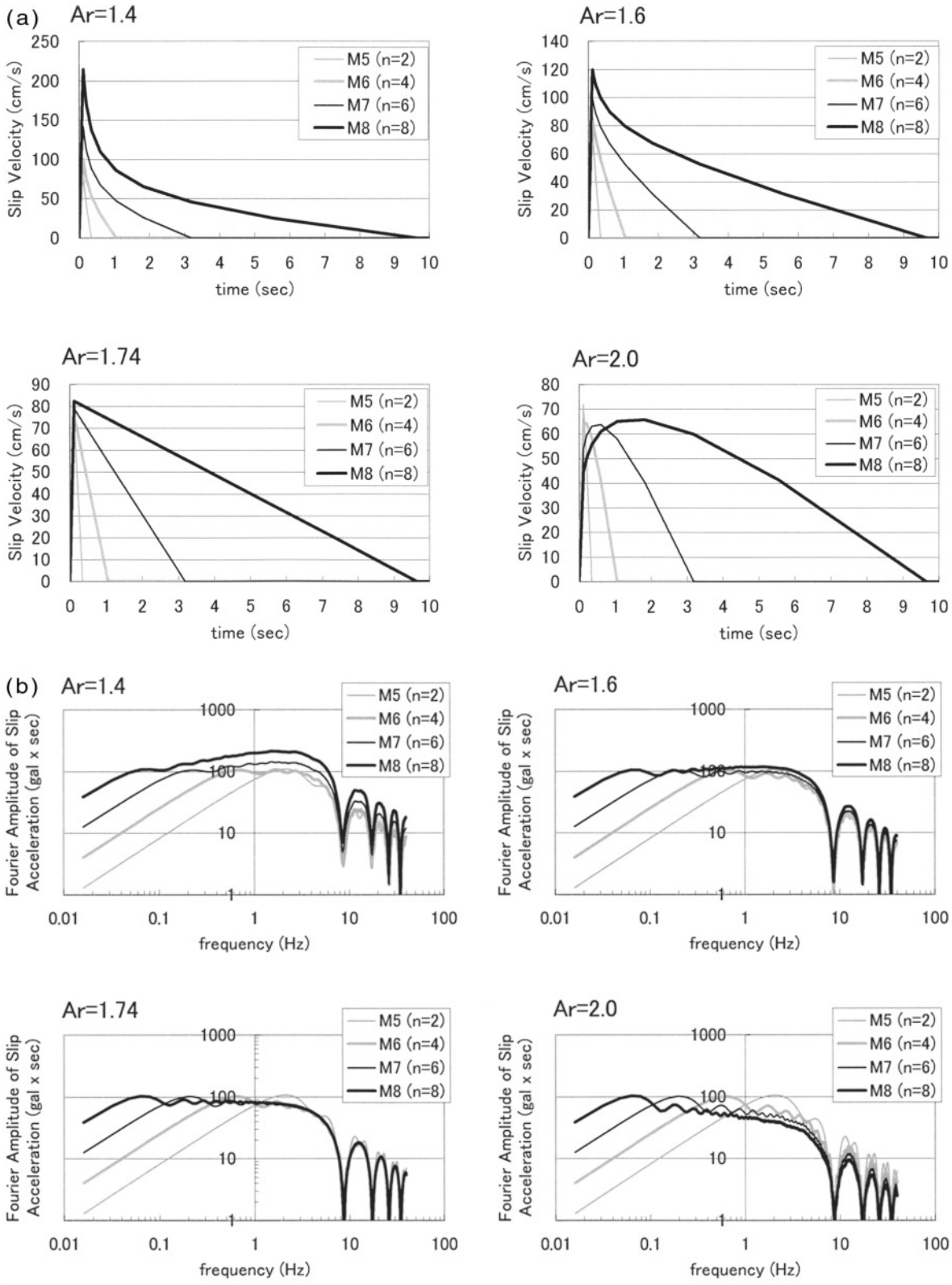

Figure 3. (a) The slip velocities and (b) the Fourier amplitudes of the corresponding slip accelerations for the case of $f_{\max} = 5$ Hz and $Tr = 1.74$.

$$f_1 \approx 1/2\tau_{max}. \quad (26)$$

Thus, $f_1 \approx 1.7$, 0.45, 0.16, and 0.052 Hz for $M = 5$, 6, 7, and 8, respectively. The second corner frequency is f_{max} (= 5 Hz).

Figure 4 shows the Fourier amplitudes of the slip accelerations of various magnitudes using the combinations of the plausible peak velocities and accelerations, whose parameters are shown as the bold values in Table 1. Note that their amplitudes are about flat between f_1 and f_{max} in all cases, meaning the Fourier amplitudes of slip velocities fall off as the inverse of ω (i.e., a ω-inversed model). This conclusion is the same as in Hisada (2000a).

In this article, I assume that the ω-inversed model of the slip velocity is true along the whole fault plane. However, this may be modified for some cases, especially a source model with surface faulting. The strong-motion records near the 1999 Chi-Chi, Taiwan, earthquake provided an excellent opportunity to investigate the slip-velocity function at various locations on the fault plane. In particular, it is interesting that the strong motions near the surface rupture (i.e., TCU052 and TCU068) lack large high-frequency waves, as compared with the regular strong motions in the epicentral area. Seemingly, the shallower parts of the fault plane (say, less than 5 km) did not excite large high-frequency waves. To interpret these effects using the slip model proposed here, f_{max} is probably very low and/or Ar may be larger than Tr. One of the advantages of the proposed model is very easy to include these effects by using variable f_{max} and/or Ar depending on depth.

Source Spectra Considering Variable Slip and Rupture Velocity

In order to investigate the effect of the 2D spatial variation of slip and rupture velocity on the source spectra, I evaluate the source spectra of 2D sources by assuming temporarily the instantaneous slip ($F_v(x_1, x_2, \bar{\omega}) = 1$) in equation (7). Neglecting the term $\mu\exp(i\omega R_0/c)$ in equation (7), the source spectra can be expressed as:

$$S(\omega) = \int_0^W \int_0^L D(x_1, x_2) \exp\left\{i\omega\left(\frac{r_s}{\overline{Vr}C_d} + \Delta t_r\right)\right\} dx_1 dx_2. \quad (27)$$

In the following, I will check the source spectra using various types of spatial variation of slip and rupture velocity. First, I will assume nondirectivity cases (i.e., $\theta = \varphi = 90°$ in equation 8) and then check its effects on the source spectra.

Source Model with Rectangular Asperities and Constant Rupture Velocity

One of the simplest asperity model would be a slip model consisting of rectangular subfaults with locally constant slips, which is commonly used in source inversion studies. As an example, I use hereafter the inversion result of the 1995 Hyogoken-Nanbu, Kobe, earthquake obtained by Yoshida *et al.* (1996). Although this earthquake consisted of two main faults (the Kobe- and Awaji-side faults), I use only the Kobe-side fault for simplicity. Figure 5 shows the slip distribution of the Kobe-side fault; the fault length and width

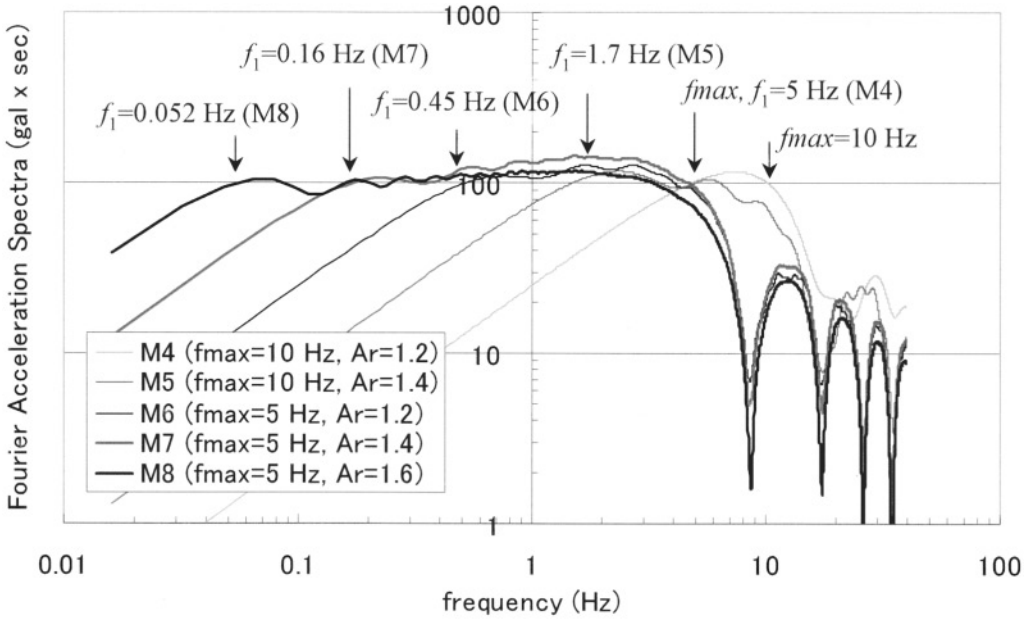

Figure 4. The Fourier amplitudes of the slip accelerations of various magnitudes using the combinations of the plausible peak velocities and accelerations, whose parameters are shown as the bold values in Table 1. Note that the velocity spectra fall off as the inverse of ω between f_1 and f_{max}.

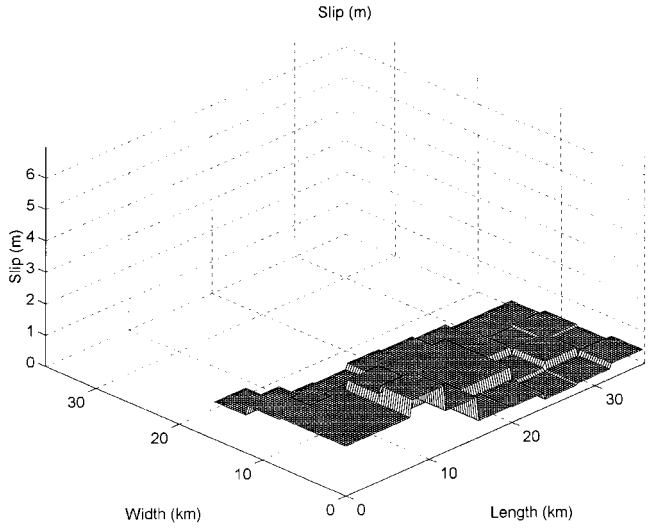

Figure 5. The slip distribution of the Kobe-side fault model by Yoshida *et al.* (1996). The fault length and width are 36 and 16 km, respectively, and the subfault size is 4 × 4 km^2.

are 36 and 16 km, respectively, and the subfault size is 4 × 4 km^2. I will assume here that the rupture velocity is constant ($\overline{Vr}$ = 2.8 km/sec and $\Delta t_r = 0$).

To compute the source integral in equation (27), I will use two different models. One model uses one integration point per subfault (model 1a); this simple integration scheme is still widely used not only in source inversion studies, but also in strong-motion simulations. The integration can be done as follows:

$$S(\omega) = \sum_{i=1}^{N_L} \sum_{j=1}^{N_W} D_{ij} \exp\left\{i\omega \frac{r_{Sij}}{\overline{Vr}}\right\} \Delta L \Delta W, \qquad (28)$$

where, N_L and N_W are the numbers of subfaults along the length and width ($N_L = 9$ and $N_W = 4$ in this model), D_{ij} is the slip of the (i, j) subfault, and r_{Sij} is the distance from the hypocenter to the center of the (i, j) subfault. Figure 6a shows the rupture time distributions for model 1a. Since the rupture velocity is infinite within subfaults, sharp discontinuities exist among adjacent subfaults in this model.

The other model uses much denser integration points to represent a continuous rupture front (model 1b),

$$S(\omega) = \sum_{i=1}^{N_L} \sum_{j=1}^{N_W} \left\{ D_{ij} \sum_{k=1}^{M_L} \sum_{l=1}^{M_W} \exp\left(i\omega \frac{r_{Sijkl}}{\overline{Vr}}\right)\right\} \Delta L \Delta W, \qquad (29)$$

where M_L and M_W are the numbers of the divided integration points on subfaults, and r_{Sijkl} is the distance from the hypocenter to the integration points. Figure 6b shows the rupture time distributions of model 1b, where $M_L = M_W = 40$ are used. Since the rupture velocity is constant and dense integration points are used, the rupture time is smoothly distributed in this model.

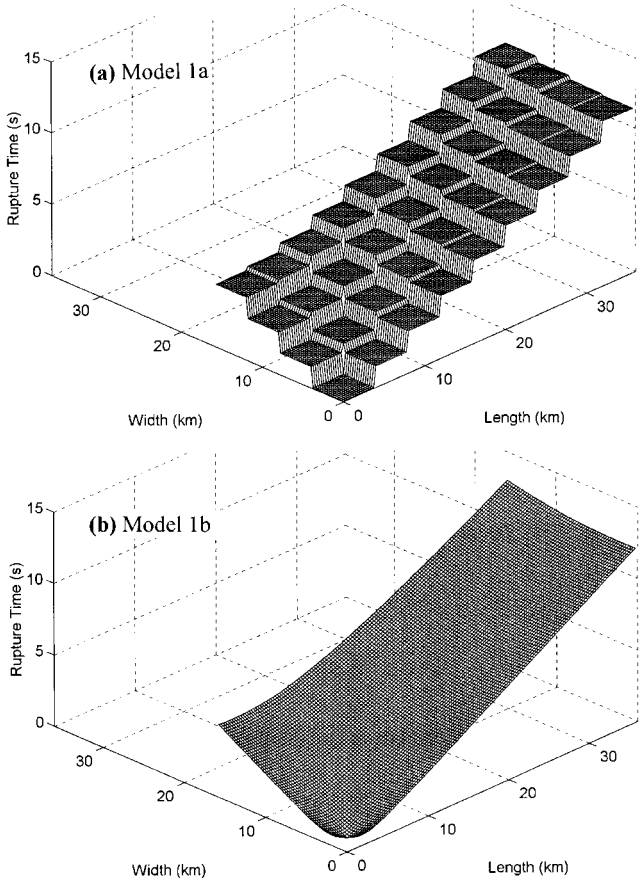

Figure 6. The rupture time distributions for (a) model 1a and (b) model 1b. In model 1a, the integration is carried out by one point per sub-fault. Since the rupture velocity is infinite within subfaults in this scheme, sharp discontinuities exist among adjacent subfaults. On the other hands, model 1b uses much denser integration points to represent a continuous and smooth rupture front.

Figures 7 and 8 show the source spectra and source–time functions of models 1a and 1b, respectively. The amplitudes of the spectra are multiplied by ω, and thus the constant amplitude represents a ω^{-1} decay. The spectrum of model 1a is roughly independent of ω showing extremely strong high-frequency amplitudes. The corresponding source–time function (i.e., the far-field displacement) shows unrealistically fluctuated high-frequency waveforms. On the other hand, the spectrum of model 1b falls off as ω^{-1}. However, its source–time function shows stopping and starting phases generated at the edges of subfaults, which also seems unrealistic.

To summarize, both models seem far from reality; the slip should not be discontinuously distributed as shown in Figure 5. Therefore, one should be careful in using this type of simple asperity models (i.e., rectangular subfaults with locally constant slips). Next I will check source models with more realistic and continuous slip distributions.

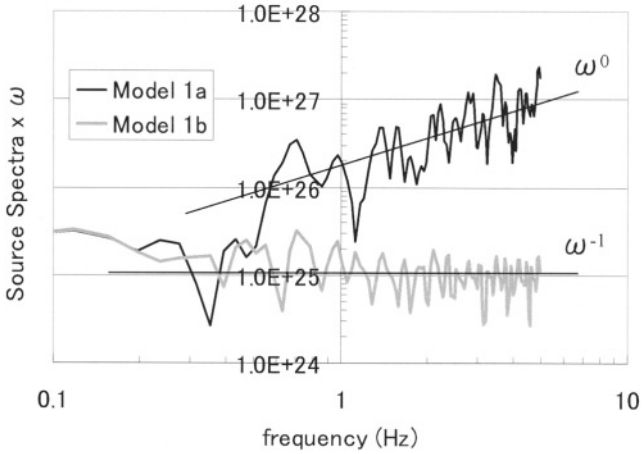

Figure 7. The source spectra of model 1a (black line) and model 1b (gray line). The amplitudes of the spectra are multiplied by ω. Therefore, the spectrum of model 1a is roughly independent of ω, whileas that of model 1b shows a ω^{-1} decay.

Source Model with *k*-Squared Slip Distribution and Constant Rupture Velocity

I will check the source spectra of the 2D *k*-squared model with a constant rupture velocity, where its spatial wavenumber spectrum of the slip distribution falls off as the inverse of the wavenumber squared (*k*-squared) (Herrero and Bernard, 1994).

Here, I propose a hybrid *k*-squared slip model in order to obtain a realistic slip distribution for the Kobe earthquake model (Fig. 9). First, at wavenumbers lower than the Nyquist wavenumbers of the subfault dimensions ($k \leq 1/2\Delta L$ for the length and $k \leq 1/2\Delta W$ for the width), I use a smooth slip distribution obtained from the source inversion result. Since the original Kobe model has an unrealistic discontinuous slip distribution (Fig. 9a), the slip is linearly interpolated (Fig. 9b), then smoothed out using a bicubic Spline intepolation (Fig. 9c).

Second, at wavenumbers higher than the Nyquist wavenumbers, I use the *k*-squared slip model based on the 2D butterworth function with random phases (e.g., Somerville, *et al.,* 1999),

$$D(x_1, x_2) = \sum_{n=1}^{N} \sum_{m=1}^{M} \frac{\bar{D}}{\sqrt{1 + (m^2 + n^2)^2}} \cos\left(2\pi \cdot m \cdot \frac{x_1}{L} + \theta_{mn}\right) \cos\left(2\pi \cdot n \cdot \frac{x_2}{W} + \theta_n\right), \quad (30)$$

where n and m are the wavenumbers normalized by the fault length and width, respectively, θ_{mn} and θ_n are random phases between 0 and 2π (radians), and $\bar{D}$ is the adjustable static slip; the total sum of the final slip over the fault plane (Fig. 9d) must be the same as the sum of the original slip (Fig. 9a) to conserve the seismic moment. The variables M and N are the maximum values for m and n, and $M\bar{V}_r/L$ and $N\bar{V}_r/W$ estimate roughly the limits of resolution in frequency.

Finally, the hybrid *k*-squared slip model is obtained by superposing the two models, as shown in Figure 9d. The source spectra of this model are calculated as follows:

$$S(\omega) = \sum_{i=1}^{N_L} \sum_{j=1}^{N_W} \left\{ \sum_{k=1}^{M_L} \sum_{l=1}^{M_W} D_{ijkl} \exp\left(i\omega \frac{r_{Sijkl}}{\overline{Vr}}\right) \right\} \Delta L \Delta W, \quad (31)$$

where D_{ijkl} is the slip at the (i,j,k,l) integration point.

The thick black line in Figure 10, as indicated by Δt = 0.0 sec, shows the source spectrum of the hybrid model assuming the constant rupture velocity ($\bar{V}_r$ = 2.8 km/sec). I generated one hundred sets of the *k*-squared model modifying the random phases in equation (30) and show their average values in the figure. The amplitudes of the spectrum are multiplied by ω, and thus, the spectrum of this model falls off as the inverse of ω-squared, as expected by the original *k*-squared model (Herrero and Bernard, 1994). Therefore, when I combine this slip model with the slip-velocity model having the ω^{-1} decay, as shown earlier, the final source spectrum falls off as the inverse of ω-cubed. The reason for the lack of high-frequency waves should be due to having neglected the spatial variation of the rupture velocity (or the rupture time) (Hisada, 2000a).

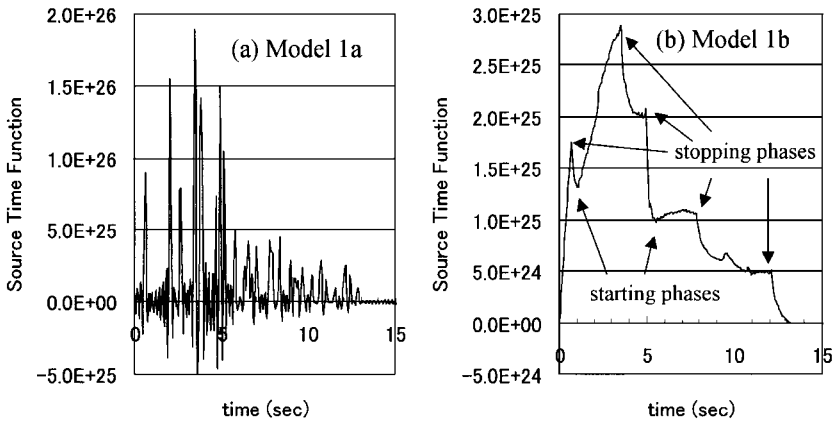

Figure 8. The source–time functions of (a) model 1a and (b) model 1b. Model 1a shows extremely strong high-frequency waves, whereas model 1b shows stopping and starting phases generated at the edges of subfaults.

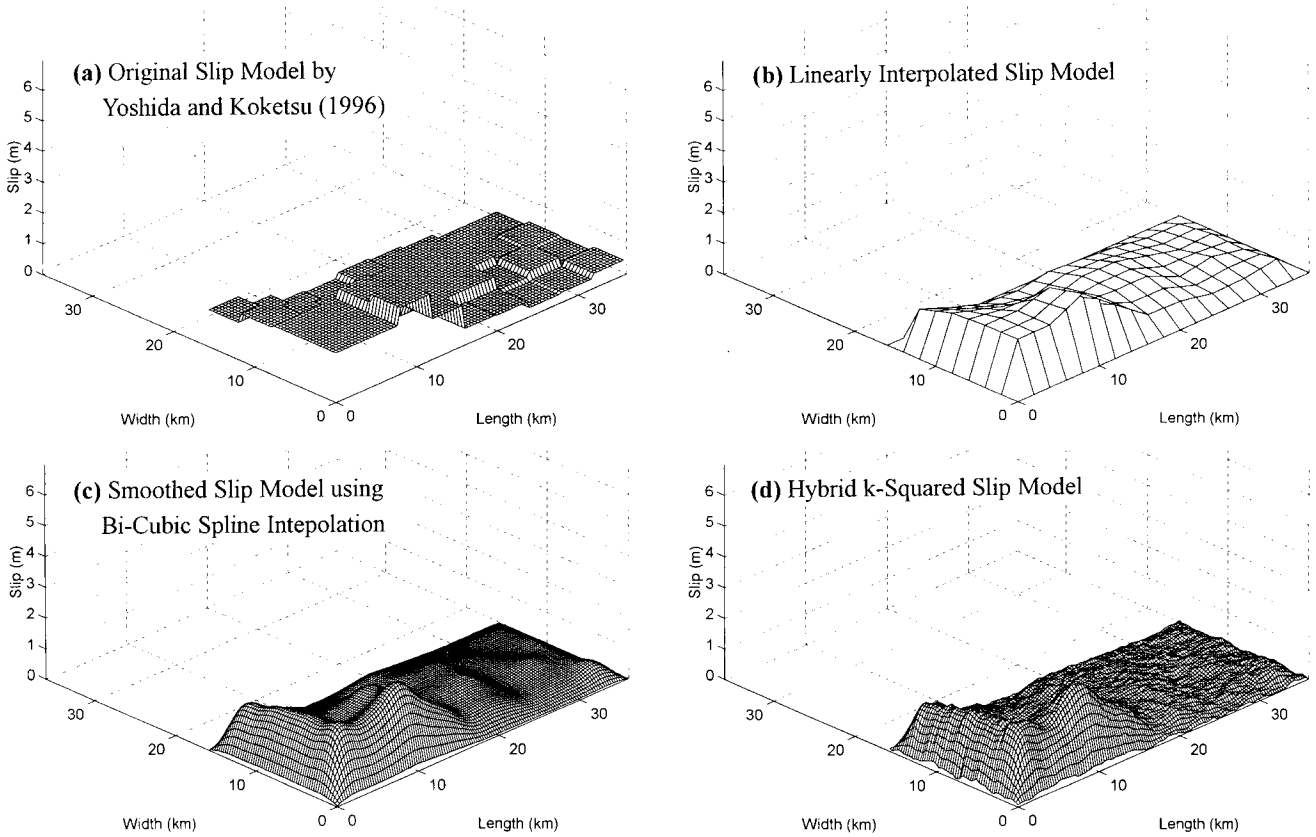

Figure 9. The construction of the hybrid *k*-squared slip model for the Kobe earthquake: (a) the original discontinuous slip distribution by Yoshida *et al.* (1996); (b) the linearly interpolated slip model; (c) the smoothed-slip model using the bicubic Spline interpolation; and (d) the hybrid *k*-squared slip model, which is the combination of model c and the *k*-squared model with random phases at the wavenumbers higher than Nyquist wavenumbers of the subfault dimensions.

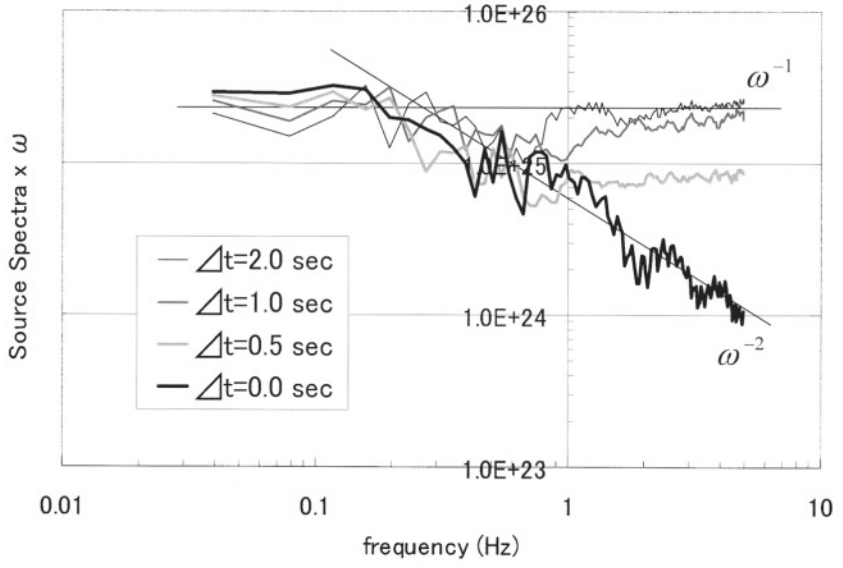

Figure 10. The source spectra of the hybrid *k*-squared models for the cases of $\Delta t = 0.0$, 0.5, 1.0, and 2.0 sec. The amplitudes of the spectra are multiplied by ω. Therefore, the spectrum for $\Delta t = 0.0$ (smooth rupture without the incoherent rupture time) falls off as the ω-squared, whereas the other spectra show ω^{-1} decays.

Source Model with *k*-Squared Distributions of Slip and Rupture Time

Here, I will check the source spectra of the hybrid *k*-squared slip model with variable rupture velocities by introducing the incoherent rupture time (Δt_r),

$$S(\omega) = \sum_{i=1}^{N_L}\sum_{j=1}^{N_W}\left[\sum_{k=1}^{M_L}\sum_{l=1}^{M_W} D_{ijkl}\exp\left\{i\omega\left(\frac{r_{Sijkl}}{\overline{Vr}} + \Delta t_{rijkl}\right)\right\}\right]\Delta L\Delta W, \quad (32)$$

where Δt_{rijkl} is Δt_r, at the (i, j, k, l) point.

I assume the *k*-squared distribution for Δt_r, as discussed in Hisada (2000a). Since I already have the *k*-squared distribution of the slip, I simply assume that the Δt_r distribution is reciprocally proportional to the slip distribution. The numerical results using dynamic source models (i.e., Day, 1982) and the observational results (i.e., Archuleta, 1982) have shown that spatial variations of peak slip velocity are strongly coupled to those of rupture velocity. Generally, one finds that the larger the slip, the larger the slip velocity. In addition, the larger Δt_r is, the slower the rupture velocity. Therefore, the model, whose Δt_r distribution is reciprocally proportional to the slip distribution, is probably better than the model whose Δt_r distribution is proportional to the slip. In fact, I have checked the latter cases, and have obtained similar results.

Figure 11 shows the rupture time distributions for the cases where the average incoherent rupture times (Δt) are 0.5, 1.0, and 2.0 sec. As compared with the model for $\Delta t = 0$ (Fig. 6b), the rupture times in Figure 11 are fluctuated rapidly. The model with $\Delta t = 2.0$ is probably not realistic because the rupture velocity exceeds locally V_S and V_P.

Figure 10 shows the source spectra using the hybrid *k*-squared slip model with the rupture time distributions shown in Figure 11. The amplitudes of the spectra are multiplied by ω. Similarly to the case for $\Delta t = 0$, I generated 100 sets of the models for Δt by changing the random phases, and their average spectra are shown in the figure. When $\Delta t \neq 0$, all the spectra show roughly ω-inverse decays. In addition, it is seen that the larger Δt is, the larger the high-frequency waves become. These conclusions are the same as those of the 1D source model (Hisada, 2000a).

The Effect of the Directivity on the Source Spectra

I will check the directivity effects on the source spectra and the corresponding source–time functions. Since I have obtained the same conclusion for every model I tried, I will show here only one example for the case $\Delta t = 1.0$ (sec), whose Δt_r distribution is reciprocally proportional to the hybrid *k*-squared slip model.

Figure 12a shows the source spectra for $\theta = 90°$ and $\varphi = 90°$ (no directivity), $\varphi = 0°$ (forward directivity), and $\varphi = 180°$ (backward directivity), whose amplitudes are multiplied by ω. As expected (e.g., Bernard *et al.,* 1996), the amplitude is larger for the forward model and smaller for the backward model. Note that all the spectra show ω-inversed decays.

Figure 12b shows the corresponding source–time functions. As compared with the model of $\varphi = 90°$, the forward

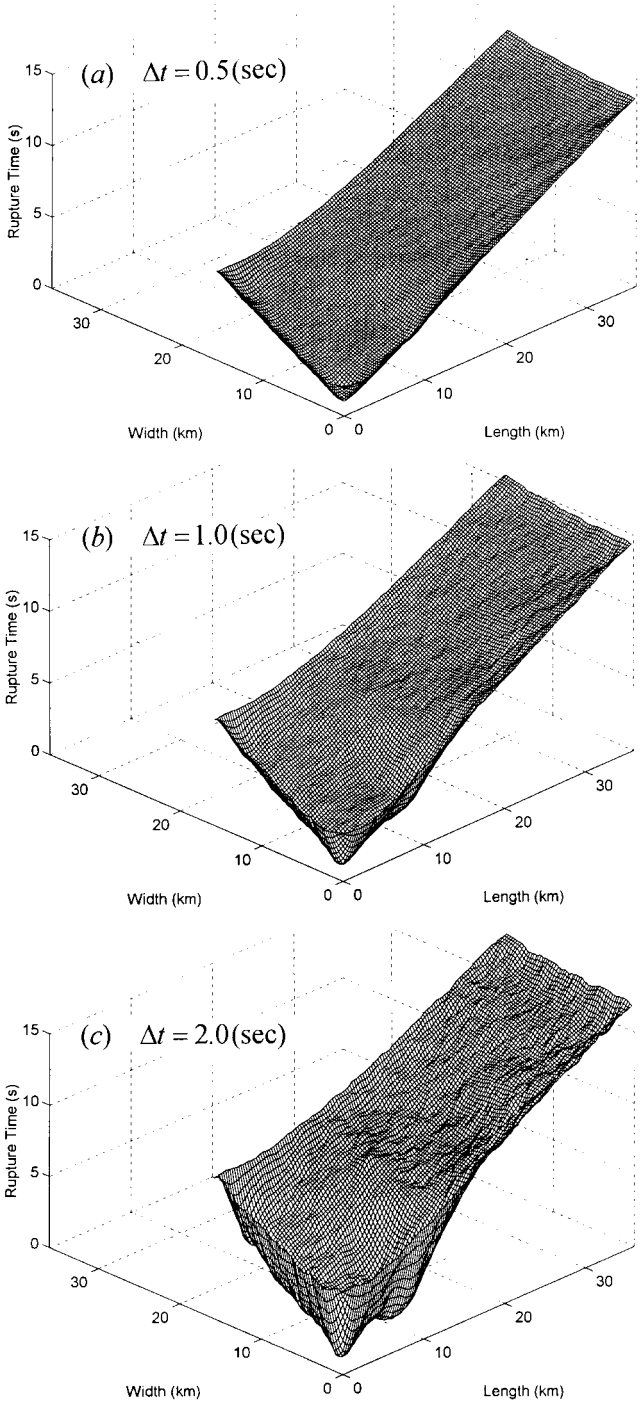

Figure 11. The rupture time distributions for the cases of the average incoherent rupture times (Δt) are (a) 0.5, (b) 1.0, and (c) 2.0 sec. I assumed that the Δt_r distribution is reciprocally proportional to the slip distribution (Fig. 9d).

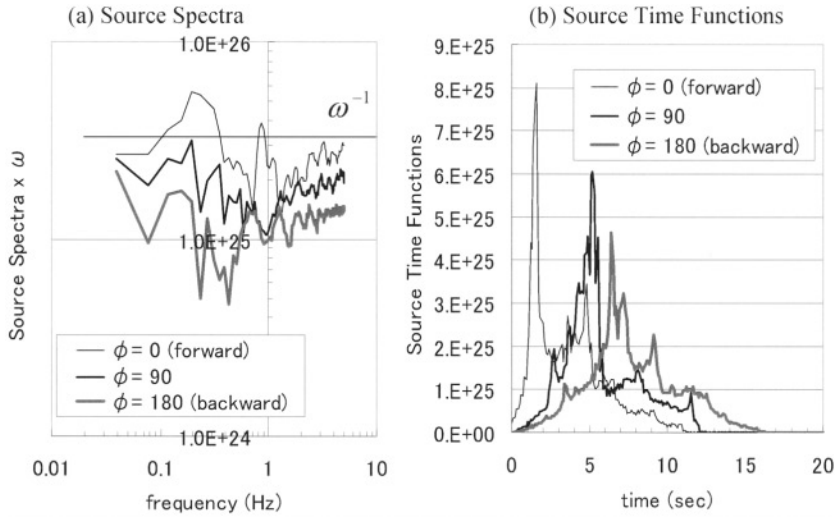

Figure 12. (a) The source spectra for φ = 90° (no directivity), 0° (forward directivity), and 180° (backward directivity) for the case of Δt = 1.0 sec, and (b) the corresponding source–time functions.

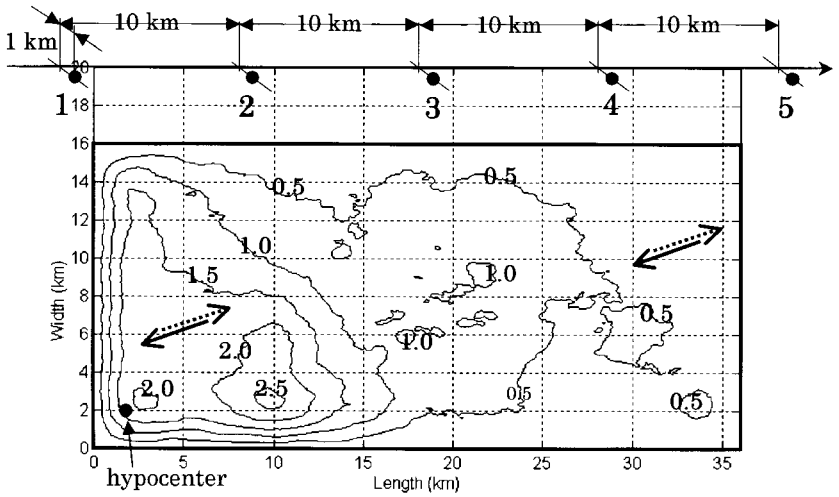

Figure 13. The fault model and five observation points for simulating near-source strong motions. The fault length (36 km) and width (16 km), and the slip distribution (the contours in the figure) are the same as those of Figure 9d. The dot and arrows on the fault plane indicate the hypocenter and the direction of the right-lateral slip.

model exhibits the larger amplitude and shorter duration, while the backward model shows smaller amplitude and longer duration.

Strong Ground Motions near Fault and Rupture Directivity Effects

Finally, I simulate broadband strong motions near a fault using equation (1) and check the rupture directivity effects using the proposed source model.

Figure 13 shows the fault model and five observation points. The fault length and width and the slip distribution of the hybrid *k*-squared model are the same as those of Figure 9d, which are originally derived from the Kobe earthquake. As shown in the figure, it is a right-lateral strike-slip fault with the dip angle of 90° and the rake angle of 210°. Its shallowest edge is located at the 4-km depth from the free surface. The contours on the fault show the *k*-squared slip distribution, and the black dot on the fault plane indicates the starting point of rupture. The five observation points line up at 1 km apart from the fault plane and at regular 10-km intervals on the free surface. Point 1 corresponds to the direction of the backward directivity, while points 3 to 5 correspond to the forward direction. As for the slip-velocity function, I use the parameters listed as the bold values for M = 7 in Table 1: $f_{\max}$ = 5 Hz, Tr = 1.74, N_V = 6, and Ar = 1.4.

As for Green's function in equation (1), I use that of the homogenous full-space and multiply the factor of 2 to take into account the free surface condition. The material properties of the medium are ρ = 2.8 t/m^3, V_P = 6.0 km/sec, V_S = 3.5 km/sec, Q_P = 500, and Q_S = 250. First, I calculate strong motions up to 5 Hz in the frequency domain and then calculate time histories using the inverse fast Fourier transform algorithm and the low-pass filter with a flat range from 0 to 4 Hz.

Figures 14a and b show the simulated accelerations, velocities, and displacements for the fault-normal and fault-

parallel components, using the smooth rupture time model ($\Delta t_r = 0$) (see Fig 6b) and the *k*-squared rupture time model ($\Delta t_r = 1.0$ sec; see Fig. 11b), respectively. It should be noted that the amplitude scales of the fault-normal components are 10 times larger than those of the fault-parallel components in all the figures. This indicates strong directivity effects at broad frequencies. The displacements in Fig. 14a and b show similar simple waveforms: smoothed step functions for the fault-parallel components and long-period pulses for the fault-normal components, whose amplitudes grow in the forward direction, as expected theoretically. On the other hand, the velocities and accelerations are very different between the two models. In particular, the accelerations in Figure 14a show simple waveforms consisting of a couple of directivity pulses. Each pulse corresponds to the asperity existing from the rupture front to the corresponding observation point (see Fig. 13). Their waveforms seem too simple to be accelerations, even though the complex *k*-squared slip distribution was considered. On the contrary, the accelerations in Figure 14b show complex random characteristics at high frequencies, which seem much more realistic. Therefore, the *k*-squared distribution of the rupture time is much more important and essential for representing realistic broadband waveforms than the *k*-squared slip distribution.

Figure 15 shows the Fourier amplitudes of the accelerations of the fault-parallel and -normal components and their amplitude ratios at three observation points (1, 3, and 5). The top three and the bottom three graphs represent the results for the smooth rupture model ($\Delta t_r = 0$) and the *k*-squared rupture model ($\Delta t_r = 1$ sec), respectively. As expected from the previous results, the Fourier amplitudes of the tops fall off as ω-cubed at the frequencies higher than the first corner frequency, whereas those of the bottoms show ω-squared models. All the amplitudes of the fault-normal components are several times larger than the corresponding parallel components, and their ratios increase from the backward rupture direction (point 1) to the forward direction (points 3 and 5). Interestingly, the amplitude ratios are roughly constant at the frequencies higher than the first corner frequency. This is contradictory to the empirical directivity models (e.g., Sommerville *et al.,* 1995), where the ratios decrease to 1 at higher frequencies. Undoubtedly, the scattering path effects should be one of the reasons for this contradiction. However, the main reason is probably due to the limitation of the 2D fault model, whose plane is flat and its radiation pattern, $e_k n_j + e_j n_k$ in equation (1), is independent of frequencies and/or wavenumbers. To represent more realistic radiation patterns and rupture directivity effects, I probably need to incorporate an empirical frequency-dependent radiation pattern (e.g., Pitarka *et al.,* 2000) or to introduce a more realistic 3D faulting model. In particular, the 3D model should be wavenumber dependent, that is, a nearly flat plane at longer wavenumbers and highly fluctuated surface or volume at shorter wavenumbers.

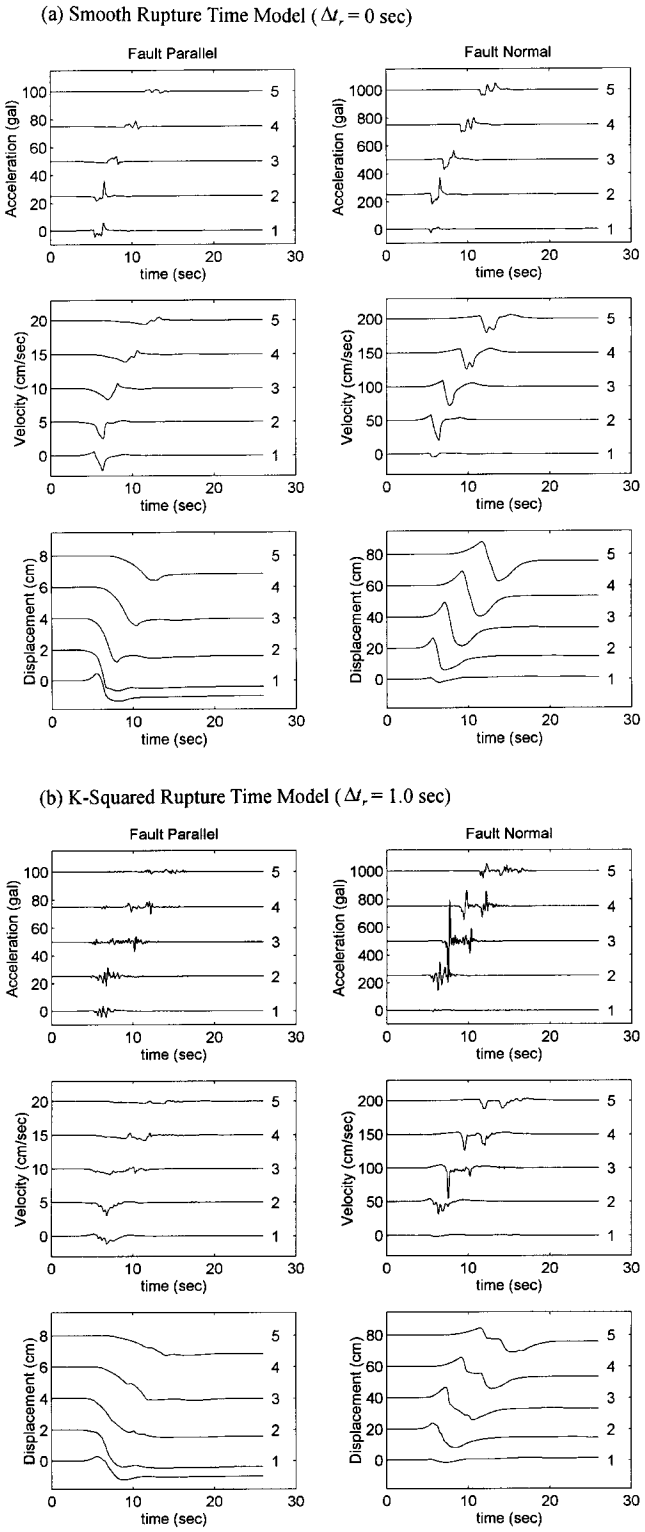

Figure 14. The simulated near-source accelerations, velocities, and displacements for the fault-normal and fault-parallel components, using (a) the smooth rupture time model ($\Delta t_r = 0$; see Fig. 6b), and (b) the *k*-squared rupture time model ($\Delta t_r = 1.0$ sec; see Fig. 11b).

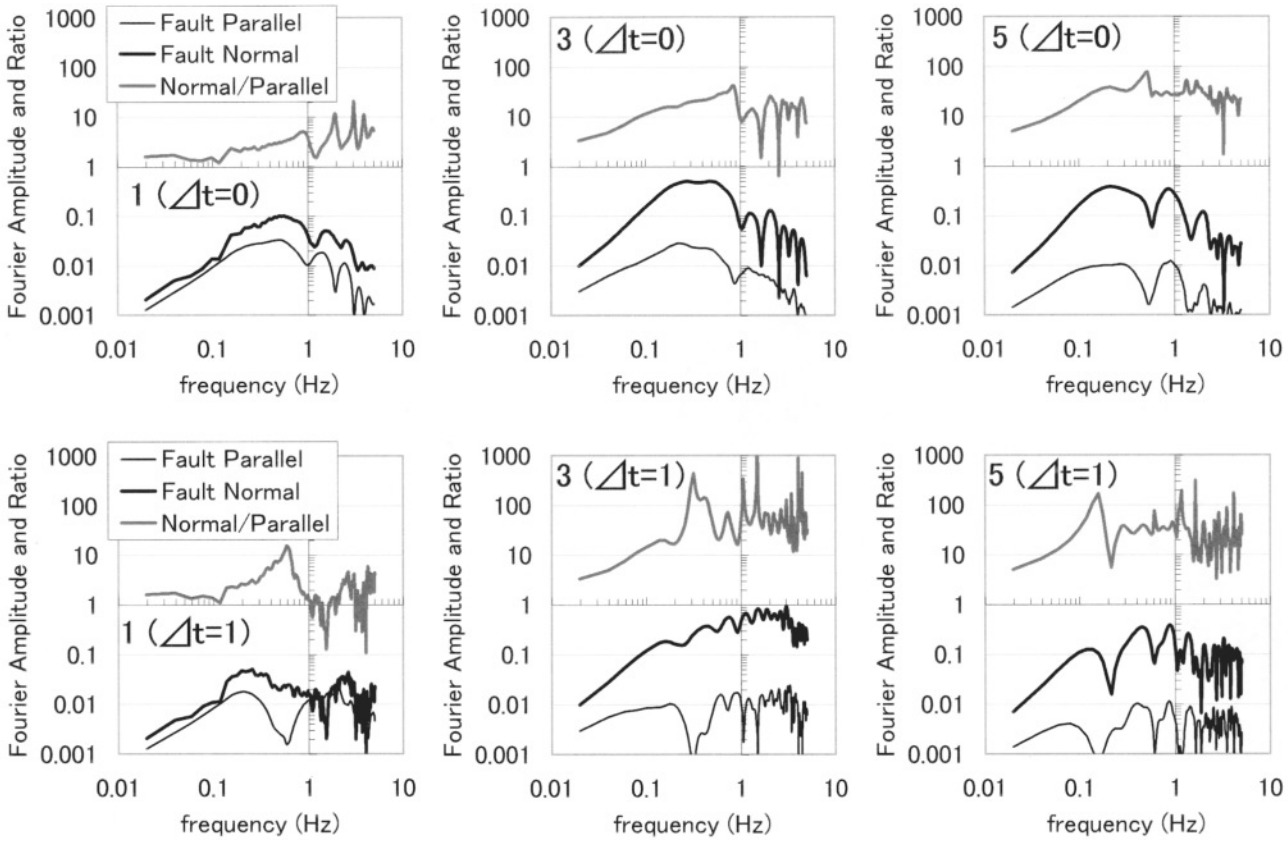

Figure 15. The Fourier amplitudes of accelerations (unit: m/sec) of the fault-parallel and fault-normal components and their amplitude ratios at three observation points (1, 3, and 5). The top three and the bottom three graphs represent the results for the smooth rupture model ($\Delta t_r = 0$) and the k-squared rupture model ($\Delta t_r = 1$ sec), respectively.

Discussion

I obtained the same conclusions as Hisada (2000a) using 2D source models. The ω-squared model consists of two ω-inversed spectra models; one is the slip velocity function, and the other is the k-squared model for the spatial distributions of slip and rupture time. Therefore, following Hisada (2000a), I shall call this model the ω-inverse-squared model.

Regarding the slip-velocity function, I generalized the previous results of Hisada (2000a) by superimposing scalene triangles to model arbitrary Kostrov-type slip velocities (Fig. 2). It was important to superimpose triangles with various durations to guarantee broadband frequency contents. Among various combinations of the parameters, I estimated the plausible combinations using the empirical relations for magnitude, average slip, and slip duration, obtaining the same conclusion as Hisada (2000a). Namely, the Fourier amplitude of the slip velocity has two corner frequencies: one is f_{max} and the other is f_1. f_{max} is the reciprocal of the minimum duration among the scalene triangles, and f_1 is nearly equal to the reciprocal of twice the total slip duration. Finally, I confirmed that the Fourier amplitude fell off as the inverse of ω between f_{max} and f_1 (see Fig. 4).

Concerning the effects of the spatial variations on slip and rupture time, I investigated the conventional asperity models and the k-squared models. The conventional asperity model, in which slips are locally constant within rectangular subfaults, is not appropriate for simulating ground motions because the discontinuities of slip along the subfault boundaries generates artificial starting and stopping phases. Thus, I proposed the hybrid k-squared slip model (see Fig. 9), which is the combination of the smoothed asperity model at low wavenumbers and the k-squared slip model at high wavenumbers. On the other hand, since it is not well known how to distribute the incoherent rupture time (Δt_r) on fault planes, the Δt_r distribution was simply assumed to be reciprocally proportional to the slip distribution. This led to the same conclusion as Hisada (2000a); namely, the k-squared distributions of slip and rupture time seem the most appropriate. In addition, the source spectra of these models fall off as the inverse of ω, when the slip velocity is the delta function.

Next, I discuss the merits and demerits of the proposed ω-inverse-squared model from the practical point of simulating strong ground motions. The advantage of this model is that it provides a sound theoretical basis for constructing

the conventional ω-squared model. Even though the subfault sizes used in source inversion studies are usually fairly large, and the corresponding resolutions are limited at longer periods (i.e., a few seconds for *M* 7, and several seconds for *M* 8 earthquakes), I can easily extend the limit of resolutions by assuming the self-similarity rule (i.e., the *k*-squared model). Therefore, it is possible to generate realistic broadband strong motions including not only the long-period coherent waves (i.e., the permanent offset and the forward directivity pulses near faults), but also the short-period random waves (i.e., accelerations), as demonstrated in Figure 14b. Even some peculiar strong motions, such as the accelerations observed in the area near the surface rupture during the 1999 Chi-Chi earthquake (i.e., TCU052 and TCU068) whose spectra are not apparently ω-squared, can be easily reproduced by using the slip-velocity function with a small f_{max} and/or a large *Ar*, as discussed earlier.

On the other hand, a disadvantage of this method is that it takes a lot of computational time at higher frequencies because very dense integration points are necessary to represent a continuous slip and rupture front. Numerical experiments show that the distance between integration points (Δd, namely, $\Delta L/M_L$ and $\Delta W/M_W$ in equation 32) should be $\Delta d \leq$ minimum wavelength/5 $\sim$ 10.

Especially, denser integration points are necessary at backward directions than forward directions to avoid artificial excitations at high frequencies. In the case of the Kobe model presented earlier, for example, I distributed 57,600 integration points (9 $\times$ 4 subfaults multiplied by 40 $\times$ 40 points) on the relatively small fault plane (16 $\times$ 36 km^2) to calculate source spectra up to 5 Hz. Thus, it is not easy to incorporate this source model with more realistic Green's function, such as those of flat-layered structures, on larger fault planes. In addition, this model does not reproduce the frequency-dependent rupture directivity effects, which are empirically known. Therefore, the fault-normal components of this model are always much larger than the parallel components at any frequencies. However, those problems would be easily remedied by incorporating this model with stochastic source methods at high frequencies and/or empirical frequency-dependent radiation patterns (i.e., Kamae *et al.,* 1998; Hisada, 2000b; Pitarka *et al.,* 2000).

Conclusions

I proposed the ω-inverse-squared model to construct the ω-squared model by considering the spatial variation in slip, slip velocity, and rupture time on 2D fault models. For the slip velocity, I generalized Hisada's model (2000a) by superposing scalene triangles to represent Kostrov-type slip velocities with arbitrary combinations of the source-controlled f_{max} and slip durations. Then, I obtained the same conclusions of Hisada (2000a); namely, the Fourier amplitude of this model falls off as the inverse of ω between f_1 and f_{max}. On the other hand, for modeling the spatial variation in slip and rupture time, I proposed a hybrid *k*-squared model, whose slip distribution consisted of the smoothed asperity model at low wavenumbers and the *k*-squared slip model at high wavenumbers. In addition, the distribution of the incoherent rupture time (Δt_r) was simply assumed to be reciprocally proportional to the slip distribution. This also led me to confirm the same conclusions of Hisada (2000a); namely, the source spectra of the hybrid *k*-squared models fell off as the inverse of ω, when the slip velocity was the delta function. Therefore, the ω-inverse-squared model, which is the combination of the proposed slip velocity and the hybrid *k*-squared distributions in slip and Δt_r, provides the theoretically solid basis of the ω-squared model.

In addition, this model successfully simulated most of the well-known characteristics of the near-fault strong ground motions at broadband frequencies: the permanent offset in displacements, the long-period directivity pulses in velocities, and the complex randomness in accelerations. In particular, I found that the *k*-squared distribution of the rupture time is much more important and essential not only for exciting high-frequency waves, but also for generating realistic randomness in acceleration waveforms. On one hand, this model did not reproduce the frequency-dependent rupture directivity effects (i.e., the fault-normal components are dominant over the parallel components only at longer periods). This is probably caused by the flat fault plane and the frequency (or wavenumber)-independent radiation pattern. This suggests that a 3D faulting model would be necessary to obtain more realistic broadband strong motions in future study.

Acknowledgments

I am grateful to Dr. Steven Day and an anonymous reviewer for helpful review and comments. Comments and suggestions by Drs. Jacobo Bielak, Sumio Sawada, Stewart Koyanagi, Tomotaka Iwata, Kojiro Irikura, Takashi Miyatake, Robert Graves, Arben Pitarka, and Paul Somerville are also greatly improved this manuscript. This research was partly supported by a special project of U.S.–Japan Cooperative Research for Urban Earthquake Disaster Mitigation (No. 11209201), Grant-in-Aid for Scientific Research on Priority Area (Category B), Ministry of Education, Culture, Sports, Science, and Technology of Japan (principal investigator: Dr. Tomotaka Iwata).

References

Aki, K. (1967). Scaling law of seismic spectrum, *J. Geophys. Res.* **72,** 1217–1231.

Aki, K. (1968). Seismic displacements near a fault, *J. Geophys. Res.* **73,** 5359–5376.

Aki, K. (1972). Scaling law of earthquake source time function, *Geophys. J. R. Astr. Soc.* **31,** 3–25.

Aki, K., and P. G. Richards (1980). *Quantitative Seismology, Theory and Methods,* W. H. Freeman, New York, Vol. 1.

Archuleta, R. J. (1982). Analysis of near source station and dynamic measurements from the 1979 Imperial Valley earthquake, *Bull. Seism. Soc. Am.* **72,** 1927–1956.

Ben-Menahem, A. (1961). Radiation of seismic surface waves from finite moving sources, *Bull. Seism. Soc. Am.* **51,** 401–435.

Bernard, P., A. Herrero, and C. Berge (1996). Modeling directivity of het-

erogeneous earthquake ruptures, *Bull. Seism. Soc. Am.* **86,** 1149–1160.

Brune, J. N. (1970). Tectonic stress and the spectra of seismic shear waves from earthquakes, *J. Geophys. Res.* **75,** 4997–5009.

Day, S. M. (1982). Three-dimensional simulation of spontaneous rupture: the effect of nonuniform prestress, *Bull. Seism. Soc. Am.* **72,** 1991–1902.

Geller, R. J. (1976). Scaling relations for earthquake source parameters and magnitudes, *Bull. Seism. Soc. Am.* **66,** 1501–1523.

Hanks, T. C., and H. Kanamori (1979). A moment-magnitude scale, *J. Geophys. Res.* **84,** 10,821–10,834.

Herrero, A., and P. Bernard (1994). A kinematic self-similar rupture process for earthquake, *Bull. Seism. Soc. Am.* **84,** 1216–1228.

Hisada, Y. (2000a). A theoretical omega-squared model considering the spatial variation in slip and rupture velocity, *Bull. Seism. Soc. Am.* **90,** 387–400.

Hisada, Y. (2000b). A hybrid method for predinctiong strong ground motion at broad frequencies near M8 earthquakes in subduction zone, in *Proc. of the Twelfth World Conference on Earthquake Engineering* Auckland, New Zealand, 30 January–4 February 2000, CD-ROM.

Kamae, K., K. Irikura, and A. Pitarka (1998). A technique for simulating strong ground motion using hybrid Green's Function, *Bull. Seism. Soc. Am.* **88,** 357–367.

Kostrov, B. V. (1964). Self-similar problems of propagation of shear cracks, *J. Appl. Math. Mech.* **28,** 1077–1087.

Nakamura, H., and T. Miyatake (2000). An approximate expression of slip velocity time functions for simulation of near-field strong ground motion, *Zisin. (J. Seism. Soc. Japan)* **53,** 1–9 (in Japanese).

Pitarka, A., P. Somerville, Y. Fukushima, T. Uetake, K. Irikura (2000). Simulation of near-fault strong ground motion using hybrid Green's functions Source, *Bull. Seism. Soc. Am.* **90,** 566–586.

Sato, R. (1979). Theoretical basis on relationships between focal parameters and earthquake magnitude, *J. Phys. Earth* **27,** 353–372.

Somerville, P. G., N. F. Smith, R. W. Graves, and N. A. Abrahamson (1995). Accounting for near-fault rupture directivity effects in the development of design ground motions, K. Karim Panahi (Editor), Honolulu, Hawaii, 23–27 July, American Society of Mechanical Engineering, Vol. 319. In *Proc. Joint ASME/JSMR Pressure Vessels and Piping Conference, Seismic, Shock, and Vibration Isolation.*

Somerville, P., K. Irikura, R. Graves, S. Sawada, D. Wald, N. Abrahamson, Y. Iwasaki, T. Kagawa, N. Smith, and A. Kowada (1999). Characterizing crustal earthquake slip models for the prediction of strong motion, *Seism. Res. Lett.* **70,** 59–80.

Yoshida, S., K. Koketsu, B. Shibazaki, T. Sagiya, T. Kato, and Y. Yoshida (1996). Joint inversion of near- and far-field waveforms and geodetic data for the rupture process of the 1995 Kobe earthquake, *J. Phys. Earth* **44,** 437–454.

Department of Architecture
Kogakuin University
Nishi-Shinjuku 1-24-2
Tokyo 163-8677, Japan
hisada@cc.kogakuin.ac.jp

Manuscript received 23 June 2000.